Geochimica et Cosmochimica Acta 389 (2025) 125–135

Contents lists available at ScienceDirect

Geochimica et Cosmochimica Acta

journal homepage: www.elsevier.com/locate/gca

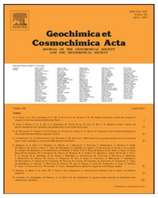

Molecular H_2 in silicate melts

Dionysis I. Foustoukos

Earth and Planets Laboratory, Carnegie Institution for Science, 5241 Broad Branch Rd. NW, Washington DC 20015, United States

ARTICLE INFO

Associate editor: Mathieu Roskosz

Keywords:
H_2
Silicate melts
Aqueous fluids
Hydrothermal diamond anvil cell experiments
Exoplanets
Primordial atmosphere
Planetary interior
Mantle
Core
Primitive chondrites
Chondrules

ABSTRACT

A series of hydrothermal diamond anvil cell experiments was conducted to constrain the equilibrium distribution of molecular H_2 between H_2O-saturated sodium aluminosilicate melts and H_2O at elevated temperatures (600–800 °C) and pressures (317–1265 MPa). The distribution of H_2 between the silicate liquid and the aqueous fluid was achieved through real-time monitoring of the H-H stretching vibration under in situ conditions using Raman vibrational spectroscopy. Results show that the solubility of H_2 in silicate melts saturated with H_2O decreases as the temperature increases, with control exerted by the mole fraction of H_2O in the melt. The dissolution of H_2 in the hydrous silicate melts appears to follow Henrian behavior, resembling that of an inert, neutral non-polar species. To express species solubility as a function of temperature (T in K) an empirical equation was developed:

$$\ln K^{m/f} = 11.4\ (\pm 1.3)\ {*}1000/T\ (K) - 18.7\ (\pm 1.1)$$

where $K^{m/f}$ is the equilibrium constant for the reaction $H_{2(g)} = H_{2(melt)}$. This equation was derived by integrating data from the current and prior experimental studies that include silicate melts with varying H_2O saturation levels. It should be deemed applicable within the temperature range of 600–1450 °C and pressures ranging from 0.3 to 3 GPa. The implications are extended into developing an understanding of the H partitioning between H_2-rich atmospheres blanketing magma oceans in the early history of planetary bodies. For example, transferring H from primordial atmospheric envelopes to the interior of rocky exoplanets may be less efficient than previously believed, which should be considered in models of volatile retention. Experimental data also suggest that minimal amounts of solar nebula H_2 are likely to dissolve in the molten surface of primitive objects in the protoplanetary disk (~10^{-5} to 10^{-9} mole faction of H_2 in the melt), contradicting the highly reducing conditions observed in chondrule mineral compositions.

1. Introduction

Numerous experimental studies have addressed the role of C—O—H volatiles on the structure and properties of silicate melts across a wide range of compositions for both the silicate liquids and coexisting phases (i.e., gas, fluid). However, the number of experiments that explore the solubility and phase equilibria of molecular H_2 as a discreet component in silicate liquids and glasses is extremely limited. Early studies primarily concentrated on the diffusion of $H_{2(g)}$ in fused silica, with results indicating a solvation mechanism that closely resembles the behavior of an inert gas adhering to Henry's law behavior when dissolving within the silicate framework (Doremus, 1966). Driven by the apparent effect of reducing redox conditions on the melting relations of the SiO_2-H_2O system (Kennedy et al., 1962), Nakamura (1974) conducted a series of SiO_2-H_2O-H_2 equilibrium experiments at 1050 °C and 1.5 GPa. It was observed that melt-fluid immiscibility was extended to higher pressures under increased H_2 fugacity (f_{H_2}). Most importantly, the liquidus behavior under varying redox conditions suggested the potential involvement of H_2 as an inert component within the system.

It was only a decade later that experimental studies further examined the solubility of molecular H_2 in silicate liquids. Luth and Boettcher (1986) investigated the impact of f_{H_2} on the silicate – fluid relations across a broad range of melt compositions, as well as under varying pressures (0.5–3 GPa) and temperatures (640–1330 °C). Their findings suggested that the solubility of H_2 in silicate liquids is considerably less than that of H_2O. They also proposed that H_2 is less involved in the melt's structure than H_2O, which might lead to H_2 exsolution as a distinct phase in H_2-saturated melts. This innovative study shed light on the possible significance of molecular H_2 dissolved in silicate liquids in shaping the redox conditions and evolutionary processes within planetary interiors.

The first quantitative data on the degree of molecular H_2 dissolution in silicate melts, defined by means of Henry's law constants, were obtained by Persikov et al. (1990). In their study, H_2 solubility in an albite melt was determined to be two orders of magnitude lower than the H_2O solubility. Additionally, they hypothesized that the H_2 solubility is independent of the silicate melt composition. Similarly, in experimental studies involving H_2O-H_2-melt equilibria for the haplogranite system,

https://doi.org/10.1016/j.gca.2024.10.020
Received 19 June 2024; Accepted 21 October 2024
Available online 26 October 2024

Schmidt et al. (1999; 1997) concluded that H_2 has lower solubility than H_2O and CO_2. The results also led them to propose that molecular H_2 functions as an inert gas within the silicate network, thereby reducing the activity of H_2O and consequently decreasing its melt solubility. The subsequent investigations of Bezmen et al. (2011; 1991) provided additional data on the solubility of H_2 in melts of similar composition. These studies also yielded further insights into the speciation of H within the silicate framework, using NMR and Raman vibrational spectroscopy.

In one of the most influential studies, Hirschmann et al. (2012) investigated the H_2 solubility in H_2O-H_2-melt systems at 1400–1500 °C, 0.7–3 GPa for melts with basaltic and andesitic compositions. By determining the Henry's law constants for H_2 dissolution in melts under a range of conditions, Hirschmann et al. (2012) proposed that H_2 exhibits a behavior similar to that of noble gases, particularly He. This observation provides additional evidence of the role of H_2 as an inert species within the silicate network. This work has been considered a major advancement in the study of planetary evolution and the transfer of H from primitive atmospheres to underlying magma oceans (e.g., Chachan and Stevenson, 2018; Young et al., 2023). Finally, Mysen (2018) conducted hydrothermal diamond anvil cell (HDAC) experiments involving in situ monitoring of melt-fluid equilibria at lower temperatures and pressures (600–825 °C; 0.6–1.4 GPa), enhancing our understanding of the molecular H_2 partitioning between silicate liquids and aqueous fluids.

Table 1
Experimental data from previous studies on molecular H_2 solubility in silicate melts.

Study	Conditions	Range of $\ln K^{m/f}$	average	stdev
Persikov et al. (1990)	1300 °C, albite $f_{H_2} = 10.2 – 865$ MPa	−10.6 to −12.8	−11.7	0.8
Bezmen et al. (1991)	1200 °C, 200 MPa, albite $f_{H_2} = 24.6 – 246$ MPa $X_w^m = 0.01 – 0.57$	−8.5 to −10.4	−9.2	0.6
Bezmen et al. (2011)	950 °C, 200 MPa, $Ab_{39}O_{32}Qtz_{29}$ glass $f_{H_2} = 26.2, 78.8, 131.3$ MPa (g24, g41, g32) X_w^m was calculated by adopting the Henry's law constant of Burnham and Davis (1974); X_w^m together with the melt wt.% ($H_2O + H_2$) was used to estimate X_{H_2} in the melt $X_w^m = 0.28 – 0.49$	−8.9 to −9.0	−9.0	0.1
Hirschmann et al. (2012)	1400–1500 °C, 700 – 3000 MPa, $f_{H_2} = 16.6 – 10411$ MPa $X_w^m = 0.02 – 0.20$	−11.43 to −13.36		
	1400 °C basaltic glass		−12.5	0.6
	1450 °C basaltic glass		−12.7	0.3
	1400 °C andesitic glass		−12.2	0.5
	1500 °C andesitic glass		−13.0	0.5
Mysen (2018)	600–825 °C, 600 – 1400 MPa, NA10 glass data are from figure 13; $K^{m/f}$ estimated from $D^{fluid/melt}$ following the equations 1–4	−6.5 to −8.3		

f_{H_2} = fugacity of H_2; X_w^m = mole fraction of H_2O in melt; X_{H_2} = mole fraction of H_2 in the melt; $K^{m/f}$ = equilibrium constant for $H_{2(g)} = H_{2(melt)}$; $D^{fluid/melt}$ = H_2 partition coefficient between fluid and melt

In spite of these studies, we still have an extremely limited understanding of the extent and mechanism of molecular H_2 dissolution in silicate melts. To address this, here I present the results of a series of hydrothermal diamond anvil cell experiments performed at 600–800 °C and pressures resembling upper mantle/lower crust environments (<1300 MPa). These experiments explored the extent of H_2 solubility in sodium aluminosilicate melts in equilibria with aqueous fluids. The data obtained together with previous experimental studies (Table 1) constrain the temperature dependence of H_2 dissolution in H_2O-bearing melts, and in the case of H_2O-saturated silicate liquids, indicate a solvation mechanism that resembles Henrian behavior, akin to that of an inert, neutral non-polar species.

2. Methods

2.1. Experimental protocols

A glass of haploandesitic composition was used as a starting material $[(Na_2Si_4O_9)_{90}{\cdot}(Na_2(NaAl)_4O_9)_{10}]$ (NA10). The glass was prepared by mixing high purity powders of Na_2CO_3, SiO_2, and Al_2O_3. The mixture was decarbonated by slow step heating (25 °C/10 min) and then melted for 2 h at 1100 °C. The composition of the synthesized glass (61.0 wt% SiO_2, 24.3 wt% Na_2O, 14.8 wt% Al_2O_3; 9.4 mol % Al_2O_3, NBO/T = 0.4) was attained by an X-ray fluorescence spectrometer (XRF-XEPOS) following procedures described by Guice et al. (2021). To enable the coexistence of H_2O-saturated silicate melt with $SiO_{2(aq)}$-saturated aqueous solutions (e.g., Mysen, 2009), at the pressure and temperature conditions of interest, the initial water/glass volumetric ratios were empirically adjusted to nearly ~1.5 based on prior experience with loading weighted NA10 glass chips in the HDAC. The loaded samples were free of entrapped air bubbles.

Reducing redox conditions and formation of $H_{2(aq)}$ was attained by the hydrothermal oxidation of native Ti metal or the decomposition of $Si_5C_{12}H_{36}$ [tetrakis(trimethylsilyl) silane, Alfa Aesar 98 %]. The abundances of the starting $Si_5C_{12}H_{36}$ and Ti metal chip were adjusted to maintain the supercritical aqueous phase free of a vapor phase, while keeping dissolved $H_{2(aq)}$ concentrations at values sufficiently high enough for in situ identification by Raman vibrational spectroscopy (Fig. 1).

Experiments were performed by utilizing an externally heated HDAC (Bassett et al., 1996). The cell was equipped with low-fluorescence 1-mm culet ultrapure synthetic diamonds to aid in Raman spectroscopy (Foustoukos, 2019), and reactants were contained in 125 μm thick Re or Ir (Exp#1; Table 2) gaskets of 500 μm diameter sample chamber. These specialized diamonds were manufactured in house by chemical vapor deposition following CIW patented methodologies (Meng et al., 2012).

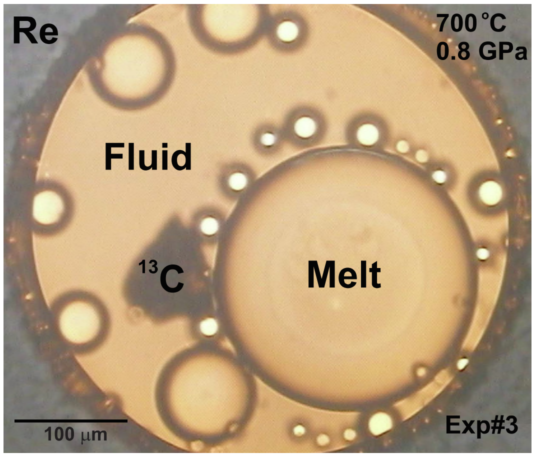

Fig. 1. Microphotography of the phases present at 700 °C, 805 MPa (Exp#3).

Table 2

Description of the HDAC experiments conducted together with the estimated equilibrium constants of $H_{2(g)}$ dissolution in H_2O-saturated silicate melts.

	T (°C)	P (MPa)	X_w^m +	$D^{fluid/melt}$	ln K_h*	ln $K^{m/f}$
			Titanium-bearing experiments			
Exp#1	800	1265	0.75	29.9 ± 0.14	−2.29	−8.67 ± 0.00
	800	1055	0.71	41.9 ± 0.84	−2.03	−8.41 ± 0.02
Exp#5	700	490	0.62	3.51 ± 0.21	−1.69	−5.14 ± 0.06
Exp#6	600	317	0.56	2.74 ± 0.03	−1.80	−5.15 ± 0.01
Exp#7	600	856	0.72	3.67 ± 0.33	−2.70	−7.52 ± 0.09
			$Si_5C_{12}H_{36}$-bearing experiments			
Exp#3	700	805	0.69	3.91 ± 1.48	−2.15	−6.31 ± 0.38
	700	840	0.70	3.08 ± 0.30	−2.20	−6.19 ± 0.10
	600	762	0.70	1.70 ± 0.07	−2.56	−6.42 ± 0.04
Exp#4	700	n.d.	n.d.	3.20 ± 0.15	n.d.	n.d.

+The mole fraction of H_2O in the NA10 melts estimated under $f_w^o = f_w^m$ conditions by adopting the model of Burnham and Davis (1974).

*Henry's law constant for the $H_{2(g)}$ dissolution in H_2O (Sverjensky et al., 2014).

n.d.: not determined.

The reducing redox conditions established at high pressures and temperatures prevented the oxidation of Re gasket. This was evident by the absence of spectral features at ~960–970 cm^{-1} in the vibrational spectra of melt and fluid phases (Fig. 2) that could have been attributed to the distinctive stretching vibration of Re-O bond for oxidized Re aqueous species (i.e., ReO_2^-. ReO_4^-) (Cheng et al., 2023; Foustoukos and Mysen, 2015). All experiments were carried out by first bringing the reactant phases to the highest temperature (e.g., 800 °C) of interest, followed by immediate spectroscopic measurements. The temperature was then lowered to the next temperature of interest. The sample remained at each pressure and temperature condition for over 2 h. Previous experimental studies have demonstrated that complete hydrothermal oxidation of Ti metal and decomposition of $Si_5C_{12}H_{36}$ occurs within minutes at these temperatures (Foustoukos and Mysen, 2012, 2013). Replicate experiments were included in the present study.

The diamond seat assembly was composed of a tungsten-sintered silicon carbide (UltraSIC, SC-30, Coorstek) that exhibits substantially greater hardness (26,000 MPa) and thermal conductivity (150 W/m K) than the tungsten carbide. The SC-30 diamond seats allow HDAC experiments to be conducted at a temperature up to 1200 °C, and pressure of 3000 MPa with maximum operational temperatures of nearly 1600 °C (Foustoukos and Mysen, 2015). A molybdenum wire was placed around the silicon carbide seats to heat the entire sample chamber. Temperature was monitored with chromel–alumel thermocouples in contact with the upper and lower diamonds (±1 °C accuracy).

Raman vibrational data were collected with a JASCO NRS-3100 confocal microRaman spectrometer with an excitation laser line operating at 490.2 nm (Coherent GENESIS MX-488) a maximum operating power of 37 mW imposed on the sample. Signal detection was accomplished through a 50X/0.42 objective lens (Plan Apo SL, Mitutoyo). The beam diameter was nearly 1 μm with a 10 μm focal depth. The acquired spectral windows were centered at 850 cm^{-1} and 3500 cm^{-1} with a frequency resolution of <1 cm^{-1} and <4 cm^{-1} at 2400 and 1200 grooves/mm, respectively. The signal was collected with a Peltier-cooled CCD at −69 °C (Andor™ Model DV401-F1 1024x128 pixel with 25 μm pixel size). The system was equipped with a holographic notch filter. All the Raman spectra collected were unpolarized. Acquisition time ranged from 5 to 120 sec/CCD window depending on the signal intensity and volatility of the analyte. Two acquisitions per window were collected.

Pressure was determined in situ by utilizing the temperature/-pressure dependent Raman frequency shift of a synthetic ^{13}C diamond (Schiferl et al., 1997). For the precise frequency measurements (± 0.1 cm^{-1}) of the fundamental band of ^{13}C, a series of acquisitions was performed at 2400 grooves/mm of the holographic gratings with the resulted Raman shift normalized to the Ne emission lines recorded on the same spectroscopic window. The Ne emission lines at 540.06 nm ($\lambda_{ex} = 490.2$ nm) were used as an internal standard for the position of the spectrophotometer (Bassett et al., 1996; Schiferl et al., 1997). To describe the temperature/pressure dependence of the Raman frequency shift of the ^{13}C diamond, an empirical regression model was employed. This model has been calibrated for low-pressure conditions (≥20 MPa) (Foustoukos, 2019) based on the experimental data of Mysen and Yamashita (2010).

Curve-fitting of the Raman spectra was performed using the commercial software IGOR from Wavemetrics™. Background subtraction was conducted by fitting a third-order polynomial function through portions of the spectra with baseline signal intensity only (Long, 1977). The integrated areas and full width at half height (FWHH) of the Raman bands (i.e., H-H ν_1) reflected the average values between Lorentzian and Gaussian fitting functions. Most of the recorded spectra for molecular H_2, however, were described by a Lorentzian function that reflects the narrowing of the H-H vibron band in H_2-enriched aqueous solutions (Foustoukos and Mysen, 2012, 2013). Many replicate measurements were acquired at the same beam spot and with the same instrumental parameters to minimize and constrain the uncertainties on spectral analysis and processing. These replicate measurements also served as time series data and provided evidence that chemical equilibration was reached in less than 2 h at temperatures higher than 600 °C (see later in discussion). Analytical errors shown represent either the standard deviation between replicate measurements or the uncertainty estimated for each individual peak integration; whichever is larger.

The statistical treatment of experimental data was performed by utilizing XLisp-Stat in the technical graphic and data analysis software Arc 1.06 (http://www.stat.umn.edu/arc) (Cook and Weisberg, 1999). For the weight on least-squares fittings the 1/(analytical error) ^{2} and the error in fit parameters was derived from the covariance matrix as SQRT (cov_{ii}), reflecting deviation of 2σ (95.4 % confidence interval) (York, 1969). The least-squares fittings were considered statistically significant if the two-tail probability (*p-value*) was of 0.05 or less (Cook and Weisberg, 1999; Devore, 1995; Press et al., 2007).

2.2. Calculating the properties of H_2O-bearing sodium aluminosilicate melts

To estimate the properties of sodium aluminosilicate melts associated with the effects of H_2O dissolution in the melt structure, the theoretical approach developed by Burnham and Davis (1974) was adopted. The regression fitting models developed (Tables S1 – S3) apply to conditions under which the fugacity of H_2O (f_w^o) is equal to the fugacity of H_2O in the melt (f_w^m). The fitted parameters were extracted from the Figures 8–12 of Burnham and Davis (1974).

To facilitate future studies, regression models were also developed to describe the Henry's law constant (*k*) of H_2O dissolution in the melt as a function of H_2O density (Table S4; Figure 13 in Burnham and Davis (1974)). The *k* constant is used to estimate the f_w^m as a function of mole faction of H_2O in the melt (X_w^m) by following the equations 20 and 21 in Burnham and Davis (1974).

The thermodynamic and phase relations discussed in Burnham and Davis (1974) have been developed for the $NaAlSi_3O_8$-H_2O system. However, this model seems suitable for constraining H_2O solubility in a wide range of silicate melt compositions (Holloway and Blank, 1994; Schmidt et al., 1999). The empirical models of Moore et al. (1995, 1998) were not used because they apply to pressures lower than 300 MPa.

The thermodynamic data of $H_{2(aq)}$ and the equation of state for H_2O (unless stated otherwise) are derived from Sverjensky et al. (2014). The standard state for liquid H_2O is unit activity at the temperature/pressure conditions of this study (Aranovich and Newton, 1996; Foustoukos, 2016a).

3. Results

3.1. Raman Spectra

Six hydrothermal diamond anvil cell experiments were conducted (Table 2) to constrain the equilibrium distribution of molecular H_2 between a H_2O-saturated sodium aluminosilicate melt and pure H_2O at high temperatures (600–800 °C) and pressures (317–1265 MPa) (Fig. 1). Phase equilibrium was initially approached from the highest temperature and pressure conditions.

Raman spectra acquired in situ revealed molecular H_2 dissolved in the reactant phases identified by the primary Raman oscillation of H-H ν_1 registered at ~4130 cm^{-1} with a FWHH of ~20 cm^{-1} and 30 cm^{-1} in the fluid and melt phase, respectively (Fig. 2a). These spectral features of the H-H stretching vibron are consistent with previous HDAC studies (Foustoukos and Mysen, 2012; Mysen, 2018; Williams et al., 2002). Formation of H_2 was observed as a product of Ti metal hydrothermal oxidation, and also during $Si_5C_{12}H_{36}$ decomposition. The latter also resulted in the formation of CH_4 documented by the distinct presence of C—H stretching vibration at ~2912 cm^{-1} with FWHH of ~26 cm^{-1} (Fig. 2a) (e.g., Dalou et al., 2022; Foustoukos and Mysen, 2013). However, the intensity of the C—H ν_1 was significantly more prominent in the spectra of the fluid phase relative to the coexisting melt (Fig. 2a), hindering in this way efforts to constrain the equilibrium distribution of CH_4 between the two phases. No other C—H volatiles or aqueous dissolved species were identified. Hydrothermal oxidation of Ti metal resulted in H_2 concentrations large enough to register the H-H Q vibrational branches in both the melt and fluid phase (Foustoukos and Mysen, 2012; Mysen, 2018; Teal and MacWood, 1935; Veirs and Rosenblatt, 1987; Williams et al., 2002).

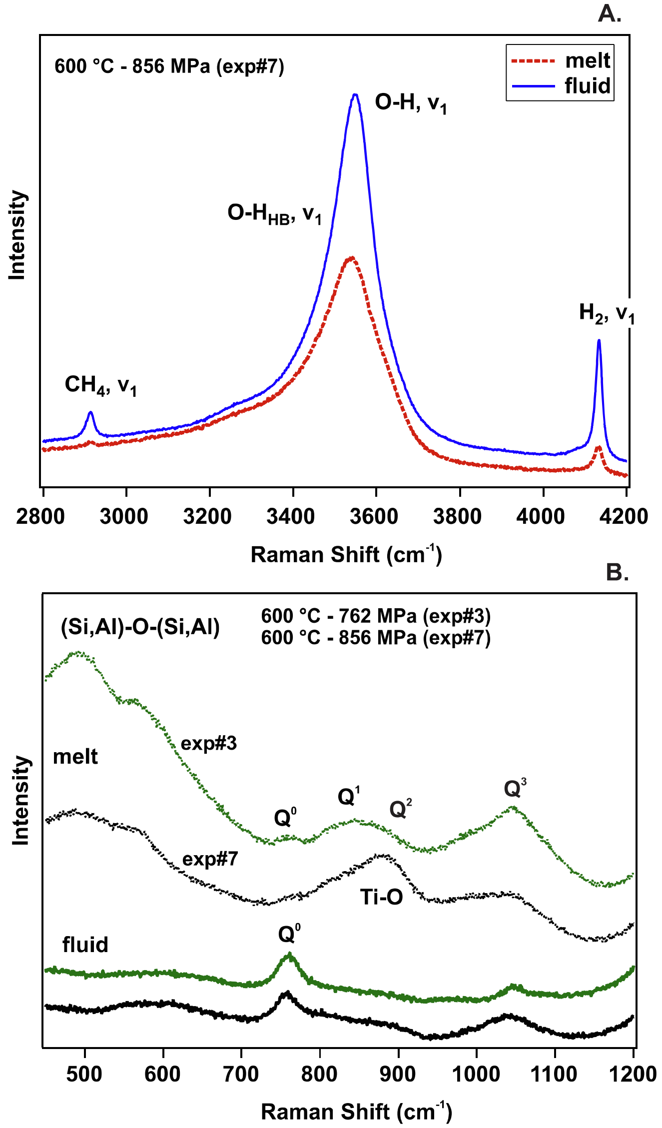

Fig. 2. Representative Raman spectra of melts and fluids coexisting at elevated temperatures and pressures. A) Molecular H_2 and CH_4 were the volatiles dissolved in the H_2O-saturated melts and aqueous solutions. Differences in the spectral features between reactant phases were employed as a means of phase identification. B) The Si-O and Ti-O speciation observed in the structure of silicate melts is consistent with previous experimental studies involving NA10 melt – fluid equilibria (Mysen, 2010, 2012, 2013b).

The replicate experiments were performed to establish the equilibrium distribution of H_2 between melts and fluids regardless of the H_2 formation mechanism. Experiments did not reveal any evidence of a distinct gas phase, indicating that volatile concentrations (i.e., H_2, CH_4) were below gas saturation at these pressures and temperatures consistent with previous theoretical and experimental studies (Sverjensky et al., 2014; Vlasov et al., 2023). Because of the lack of redox controls, determining the exact concentrations of H_2 in the aqueous phase was not workable. However, based on previous experimental studies that utilized similar redox controls and low-fluorescence ultrapure CVD diamond anvils (Foustoukos, 2019), it is highly probable that the concentrations exceeded values of 10 mM.

Other spectral features observed correspond to vibrons attributed to O—H, Ti—O and (Si—Al)—O bonds associated with the presence of H_2O, Ti-bearing (with experiments #1, #5, #6, #7) and Na-Al-silicate species dissolved in the fluid and melt (Fig. 2b). Consistent with previous experimental observations involving NA10 melt-fluid equilibria (Mysen, 2010, 2012, 2013b), the H_2O-saturated melts were enriched with a range of silicate species (Q^n, n = number of bridging oxygen) (Table S5, Fig. S4) proposed to describe the Si—O—H network in melt structure (see details in Mysen and Richet, 2005). The coexisting aqueous fluid was enriched in dissolved H_4SiO_4 (i.e., Q^0, ~760 cm^{-1}, Mysen, 2013a; Zotov and Keppler, 2002) (Fig. 2b). In the Ti-bearing experiments, evidence of Ti—O stretching vibration in the melts (~880 cm^{-1}) supported the presence of TiO_n (n = 4 or 5) complexes in the structure of NA10 hydrous melts (Mysen, 2012). This is also the case for the Raman spectra of H_2O, where the two major contributions of isolated O—H and hydrogen bonded O—H groups were observed within the frequency envelope of 3200–3800 cm^{-1}. As shown previously, the O—H vibrational spectra of H_2O solutions exhibit smaller FWHM relative to those from H_2O-enriched silicate melts because of the added contributions from structural O—H and hydrogen bonding environments associated with the Na-Al-silicate melt networks (M•••O-H, Si-O[H]-M; M = Al, Na) (Cody et al., 2005; Le Losq et al., 2015; Le Losq et al., 2017; Mysen and Virgo, 1986). Similar contributions have been observed in highly ionic Na-Mg-bearing aqueous solutions, however with a much less prominent feature associated with M•••O-H contributions (Foustoukos, 2016b). These distinct differences in the O—H spectral features between the melt and aqueous fluid were used to facilitate phase identification, complementing direct optical observations.

3.2. Equilibrium partitioning of H_2 between fluid and melt

A reaction time of over 2 h was allowed for each experimental condition. Time series measurements indicated that the solubility of H_2 in the coexisting melt and fluid achieved equilibrium. Previous experimental studies have showed that comparable reaction times establish equilibrium for the dissolution of H_2 in pure H_2O and NA10 silicate melt at these temperatures and pressures with no apparent diffusion of gas through the Re gasket (Foustoukos and Mysen, 2012; Mysen, 2018).

To constrain the extent of H_2 solubility in the H_2O-saturated NA10 melt, the integrated peak areas of the H-H stretching vibrations observed in the fluid ($A^{fluid}_{H_2}$) and melt ($A^{melt}_{H_2}$) phases are used to describe the partition coefficient ($D^{\mathrm{fluid/melt}}$) as follow:

$$D^{fluid/melt} = A^{fluid}_{H_2} / A^{melt}_{H_2} \tag{1}$$

This quotient of the integrated Raman peak areas can be considered identical to a partition coefficient associated with species concentrations under the assumption that the relative normalized differential Raman scattering cross sections of H-H (σ_{H_2}) are the same for H_2 dissolved in the H_2O-saturated melt (~ 0.7 mole fraction of H_2O in melt, Table 1) and the aqueous fluid. This assumption has been evaluated for the case of H_2O (O—H ν_1), CH_4 (C—H ν_1), NH_3 (N—H ν_1) and H_2 (H—H ν_1) in previous melt-fluid equilibria studies (Foustoukos and Mysen, 2015; Mysen, 2013a, 2018) that documented the similarity in the thermodynamic properties of H_2O solvating in the coexisting phases. However, further experimental studies are truly needed to support this assumption under a range of fluid-melt density conditions.

Results revealed that $D^{\mathrm{fluid/melt}}$ ranged from 1.7 to 41.9 with lower values attended at higher temperatures and pressures (Table 2). This indicates that molecular H_2 solubility in H_2O-saturated silicate melts coexisting with aqueous fluids tends to decrease with increasing temperature, which overall, is consistent with the quenched glass measurements of Hirschmann et al. (2012) involving basalt/andesite – fluid equilibria under reducing conditions at 1400–1450 °C, 0.7–3 GPa and with the in situ observations of Mysen (2018), where hydrous NA10 melts equilibrated with H_2-enriched fluids at 525–825 °C, 0.6–1.4 GPa.

4. Discussion

4.1. Solubility of molecular H_2 in melts – thermodynamic constraints

To constrain the thermodynamic properties of molecular H_2 solubility in H_2O-bearing silicate melts, the equilibrium relationship between $H_{2(g)}$ and $H_{2(\mathrm{melt})}$ in the coexisting phases is expressed in the generalized form of:

$$H_{2(g)} = H_{2(melt)} \tag{2}$$

with the equilibrium constant defined as:

$$K^{m/f} = X_{H_2} / f_{H_2} \tag{3}$$

where X_{H_2} is the mole fraction of H_2 dissolved in the silicate melt and f_{H_2} is the fugacity of $H_{2(g)}$ dissolved in the aqueous phase. This approach assumes ideal mixing for $H_{2(\mathrm{melt})}$ that allows the activity of $H_{2(\mathrm{melt})}$ to be equal to the X_{H_2} ($a^{melt}_{H_2} = X_{H_2}$) (Anderson and Crerar, 1993). To derive the equilibrium constant $K^{\mathrm{m/f}}$ from the experimentally determined $D^{\mathrm{fluid/melt}}$ (Table 2), the reaction (2) is combined with the equilibrium reaction of $H_{2(g)}$ dissolution in pure H_2O:

$$H_{2(g)} = H_{2(aq)} \tag{4}$$

The Henry's law constant that describes the above reaction (K_h) is then integrated with the $D^{\mathrm{fluid/melt}}$ in the form of $K^{\mathrm{m/f}} = K_h/D^{\mathrm{fluid/melt}}$ (Table 2). These estimations assume that: i) the activity coefficients of molecular H_2 dissolved in the coexisting fluid and melt phases are equal to one, ii) ideal mixing of H_2 (i.e., $D^{\mathrm{fluid/melt}} = K^{\mathrm{fluid/melt}}$) and iii) that the melt composition was not substantially deviated from the starting glass composition (NA10). The latter is in question especially for the $Si_5C_{12}H_{36}$-bearing experiments. However, the similar values of $D^{\mathrm{fluid/melt}}$ observed in all the experiments at 700 °C (Table 2), supports the validity of this assumption.

The estimated values of $K^{\mathrm{m/f}}$ appear to exhibit a linear dependence, with temperature expressed as the function of ln $K^{\mathrm{m/f}}$ with 10^3/T(K), especially when previous experimental data are considered (Bezmen et al., 2011; Bezmen et al., 1991; Hirschmann et al., 2012; Mysen, 2018; Persikov et al., 1990) (Fig. 3; Table 1). This linear correlation is strongly weighted by the experimental data of Hirschmann et al. (2012) collected at temperatures exceeding 1400 °C, however, the linear regression fitting model encompasses the experimental dataset as a whole. For example, the earlier study of Persikov et al. (1990) on albitic melt – H_2O equilibria yielded data that correspond to ln $K^{\mathrm{m/f}}$ values of -11.7 ± 0.8, which is in close agreement with the empirical model developed here. The larger deviations estimated for the experimental data of Bezmen et al. (2011) might be attributed to my use of empirical approximations for the mole faction of H_2O in the sodium aluminosilicate melt (X^{m}_{w}) (Burnham and Davis, 1974). A large discrepancy is inferred for the H_2 solubility in melts of rhyolitic obsidian attained at 800 °C (Gaillard et al., 2003) with estimated ln $K^{\mathrm{m/f}}$ values of -11.3 ± 0.2 in comparison to values of ∼−8.5 attained in the present study (Table 2). Gaillard et al. (2003) attributed similarly sizeable differences between their study and Persikov et al. (1990) to the substantially lower f_{H_2} conditions (<7 MPa) attained relative to the referred study (e.g., 10–865 MPa). The same argument, thus, may stand to explain the deviation of these experimental data from the empirical relationship that describes the high temperature and pressure melt-fluid equilibrium experiments (Fig. 3). To this end, only data from experiments at high f_{H_2} and f^{o}_{w} conditions were included in the model (Table 1). It is highly possible, therefore, that the Henry's law approach (Eqn 1) might not hold for conditions of low f_{H_2}, further suggesting the likelihood of an array of mechanisms for the solution of H_2 in the structure of silicate melts (see later in discussion) (Gaillard et al., 2003).

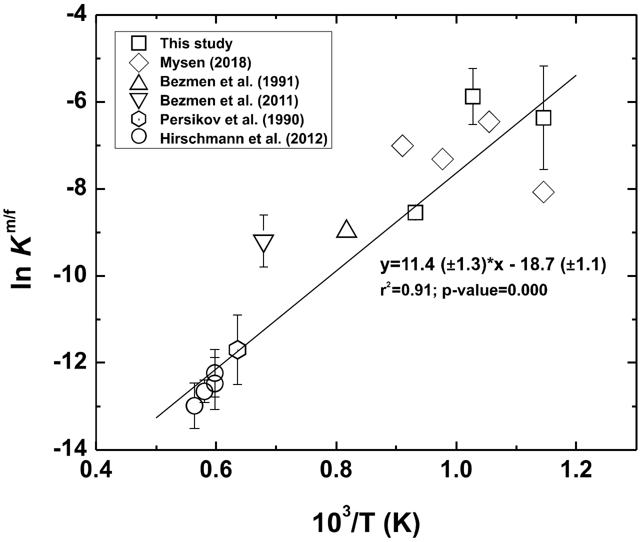

Fig. 3. Estimated values of ln $K^{\mathrm{m/f}}$ as a function of temperature for the series of experimental studies involving H_2 solubility in silicate melts. Data plotted represent the average and standard deviation values from the individual measurements at specific temperature conditions (Table 1, Table 2). This allows for the variability of ln $K^{\mathrm{m/f}}$ at each temperature to be considered in the weighted linear regression model, limiting the impact of sample size on the regression model. Data from Mysen (2018) are not included in the fitted model because they correspond to single measurements at temperature. Uncertainties not shown are smaller than symbol size.

The linear dependency of $K^{\mathrm{m/f}}$ on temperature can be further utilized to determine the thermodynamic properties of H_2 dissolution in the silicate melt:

$$\Delta_r G = \Delta_r G^o + RT\ln K^{m/f} = 0 \tag{5}$$

and when combined with:

$$\Delta_r G^o = \Delta_r H^o - T\Delta_r S^o \tag{6}$$

yields:

$$\ln K^{m/f} = -\Delta_r H^o / RT + \Delta_r S^o / R \tag{7}$$

with an empirical expression:

$$\ln K^{m/f} = 11.4\,(\pm 1.3)*1000/T(K) - 18.7\,(\pm 1.1) \tag{8}$$

where, T is temperature in Kelvin, R is the gas constant, and Δ_rG^0, Δ_rH^0, and Δ_rS^0 are the Gibbs free energy, enthalpy and entropy changes, respectively, of the reaction at standard state (25 °C, 0.1 MPa). This is a simplified approach that doesn't account for heat capacity contributions, and in generally, it should be considered applicable for the range of temperature and pressure conditions of the experimental studies adopted (600–1450 °C; 0.3–3 GPa). Based on a weighted linear regression model (Fig. 3), the estimated thermodynamic properties of $H_{2(g)}$ dissolution in a aluminosilicate melt are: $\Delta_rG^0 = -48.1 \pm 10.4$ kJ/mol, $\Delta_rH^0 = -94.5 \pm 10.8$ kJ/mol and $\Delta_rS^0 = -156 \pm 9$ J/mol•K (Table S6).

Approximating the effect of molar volume changes during $H_{2(g)}$ dissolution in the melt ($\Delta V^{melt}_{H_2}$) requires expressing ln $K^{m/f}$ as a function of pressure at constant temperature (e.g., Fine and Stolper, 1986; Foustoukos and Mysen, 2015; Hirschmann et al., 2012; Holloway and Blank, 1994; Mysen and Acton, 1999). For the experimental data of this study, the calculated $\Delta V^{melt}_{H_2}$ at 700 °C is 26 ± 5 cm^3/mol, which is nearly three times higher than the values estimated at 1400–1450 °C (Hirschmann et al., 2012). This suggests that pressure along with temperature could have a quantitative contribution to the extent of H_2 equilibria between silicate melts and aqueous fluids.

4.2. Solution mechanisms

There have been several hypotheses regarding the mechanisms that facilitate the dissolution of H_2 in silicate liquids. The role of H_2 speciation has been referred to the formation of Si—O—H and/or Si—H species (Bezmen et al., 1991; Luth and Boettcher, 1986) or to the function of H_2 more like a neutral volatile in the melt structure (Schmidt et al., 1999; Schmidt et al., 1997), or on both (Bezmen et al., 2011; Luth et al., 1987). Hydrogenation experiments of fused silica glasses conducted at 800–955 °C with f_{H_2} conditions at ~130 MPa have also suggested formation of Si-H together with Si—O—H groups in the melt structure (Schmidt et al., 1998). Similar observations in the SiO_2-H_2 system have been reported in laser – heated experiments performed at much higher pressure and temperature conditions (>1200 °C, > 2 GPa) (Shinozaki et al., 2014). Raman vibrational spectra collected in the present study at in situ conditions do not provide evidence of SiH_4 species that should have been documented by the Si-H stretching vibrons at ~2200 cm^{-1} (Schmidt et al., 1998; Shinozaki et al., 2014).

In earlier studies, the role and speciation of H_2 as molecular, Si—OH and Si—H groups in the silicate framework were studied regarding its contribution to increasing depolymerization and decreasing the solidus temperature (Luth and Boettcher, 1986). Later studies suggested these contributions are minimal in comparison with a solvation mechanism involving H_2 dominant presence in cavities as an inert volatile (Schmidt et al., 1999; Schmidt et al., 1997). This hypothesis was based on the evidence of increasing H_2 solubility with decreasing the activity of H_2O in melt, without apparent evidence of the depolymerizing species Si—O—H and Si—H. It appears, however, that the extent of H_2O solubility might depend on the f_{H_2}, with highly reducing condition decreasing the extent of H_2O solvation in the melt structure (Bezmen et al., 2011; Bezmen et al., 1991). ^{1}H NMR spectra of sodium aluminosilicate glasses quenched from melts equilibrated under elevated f_{H_2} conditions have also confirmed the presence of molecular H_2 (~ 5 ppm chemical shift) most likely confined to the interstices of the silicate network (Bezmen et al., 2011).

Here, the H_2-enriched silicate melts were saturated with H_2O, consistent with the elevated NBO/T attained in situ (Table S4), resulting in X^m_w from 0.56 to 0.78 (Fig. 4, Figure S2). However this might not be the case for previous experiments where X^m_w attained values lower than 0.57 (Table 1) (Bezmen et al., 2011; Bezmen et al., 1991; Hirschmann et al., 2012). It is hypothesized, therefore, that for the present study the contribution of H_2 into reducing the Si—O—Si structures to Si—O—H groups should be minimal, and thus, its solubility could be mostly governed by the thermodynamic properties of a species following Henrian behavior. In order words, the solvation mechanism of H_2 might be more comparable to an inert, neutral non-polar species.

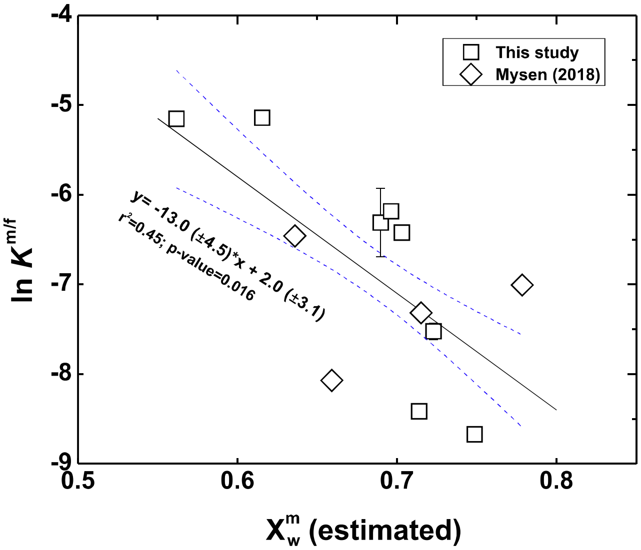

Fig. 4. Estimated values of ln $K^{m/f}$ as a function of the mole fraction of H_2O in sodium aluminosilicate melts (X^m_w) estimated when in equilibrium with H_2O solutions under $f^o_w = f^m_w$ conditions. The dissolution of H_2 as an inert, neutral non-polar species in the framework of the silicate liquid is attributed to the inverse correlation between these variables. Uncertainties not shown are smaller than the symbol size.

The solubility of $H_{2(melt)}$ appears to be controlled by the mole fraction of H_2O in the melt (Fig. 4). To constrain the X^m_w, the model of Burnham and Davis (1974) were adopted by assuming that the fugacity of H_2O (f^o_w) is equal to the fugacity of H_2O in the melt (f^m_w) for the experiments performed under H_2O-saturated silicate melt coexisting with a H_2O phase. The observed decrease of ln $K^{m/f}$ with increasing X^m_w (Fig. 4) is supportive of a dissolution mechanism attributed to a neutral non-polar species that rest in voids of the melt structure without creating bonds within the depolymerized silicate network (Schmidt et al., 1999; Schmidt et al., 1997). This, however, might not be the case for silicate glasses quenched from H_2O-undersaturated melts, such as those attained in Bezmen et al. (2011; 1991) and Hirschmann et al. (2012) where values of X^m_w of >0.5 and >0.6, respectively, are required for $f^o_w = f^m_w$ conditions. In these studies, the variability of the estimated ln $K^{m/f}$ across the range of X^m_w attained (0.02–0.49; Table 1), appears to be substantially less dependent of X^m_w (Fig. S3), suggesting that the H_2 solvation might be mainly driven by the disruption of the Si—O—Si framework and the formation of Si—O—H and Si—H bonds in the silicate liquid. Nevertheless, it is highly possible that these two different solubility mechanisms yield the same phenomenological extent of H_2 dissolution in melts across the range of temperatures investigated (600–1500 °C; Fig. 3).

To further constrain the apparent behavior of H_2 as neutral species in silicate liquids, additional insights could be drawn from the solvation mechanisms of noble gases in melts and glasses. For example, Hirschmann et al. (2012) suggested that the H_2 solubility is comparable to He based on effect of the melt ionic porosity; in other words, the abundance of voids within the silicate network (Carroll and Stolper, 1993), which could decrease volatile solubility under conditions of elevated NBO/T ratios that include both depolymerized melts and melts of mafic/ultramafic lithologies (Iacono-Marziano et al., 2010; Paonita, 2005; Shibata et al., 1998; White et al., 1989). However, the solvation mechanisms for H_2 and noble gases might differ to a great extent than previously thought. The thermodynamic properties of H_2 diffusion in silicate glasses appear to be similar to those of Ne from 25 to ~800 °C (Doremus, 1966; Lee, 1963; Shackelford et al., 1972; Shang et al., 2009; Zhang and Ni, 2010), in a fashion that follows the molecular radii of noble gases and H_2 (Press, 2016). However, as temperatures increase, the solubility of these molecular gases in silicate liquids becomes decoupled, with H_2 demonstrating a decrease in solubility as temperature rises (Fig. 3) while noble gases follow an opposite temperature dependency (Hayatsu and Waboso, 1985; Iacono-Marziano et al., 2010; Shibata et al., 1998). This is clear when examining the thermodynamic drive for melt solubility described by the range of Δ_rG^0 and Δ_rH^0 estimated experimentally for these volatiles (Table S6, Hayatsu and Waboso, 1985; Lux, 1987; Montana et al., 1993; Shibata et al., 1998). One explanation for these differences is the impact of molecular H_2O on the speciation of H dissolved in the silicate network (e.g., Fig. S3). To my knowledge, there is only one experimental study accessing He solubility in H_2O-bearing silicate melts (Paonita et al., 2000), with experimental and theoretical data suggesting an increase of noble gases melt solubility under elevated X_w^m (Nuccio and Paonita, 2000). It is quite possible, therefore, that the solvation mechanism and thermodynamic drive for noble gases dissolution in the silicate framework are quite distinct between anhydrous and H_2O-enriched silicate melts. Under similar assumptions, one can also suggest that the solubility of molecular H_2 in anhydrous silicate liquids increases with temperature in a fashion following the behavior of noble gases. Nevertheless, further experimental studies are needed to constrain noble gases solubility in the silicate melt framework under in situ pressure and temperature conditions.

4.3. Implications for H_2-rich atmospheres

Early experimental studies focused on the role of molecular H_2 in the melting point of silicates, together with the overall effect of H-bearing speciation on the structure of silicate frameworks (Bezmen et al., 2011; Bezmen et al., 1991; Luth and Boettcher, 1986; Persikov et al., 1990; Schmidt et al., 1999; Schmidt et al., 1997). Studies have also delved into the role of H_2 dissolved in silicate liquids in controlling the redox conditions and evolutionary process of planetary interiors; in particular, the role of H_2-enriched atmospheres in transferring H to planetary cores during formation (Hirschmann et al., 2012; Luth and Boettcher, 1986). This pioneering concept has become an integral aspect of modeling planetary evolution, driven by the rapid progress in exoplanet exploration (Lissauer et al., 2023; Mordasini and Burn, 2024; Weiss et al., 2023). In the absence of plate tectonics, perhaps the most straightforward way to transfer H from the atmosphere into the planetary interior is when there is a rapidly convecting magma ocean (e.g., following a giant impact, Canup, 2012). A quantitative description of the H partitioning between H_2-enriched atmospheres and underlying magma oceans necessitates the utilization of complex theoretical models, which involve rigorous thermodynamic calculations to establish the distribution of C—O—H—N—S volatiles and the redox conditions throughout the planetary interior during formation and cooling of the magma ocean. Key factors in this approach are the solubility behavior of H_2/H_2O in silicate magmas and the extent at which molecular H_2 can be transferred from the gas phase (atmosphere) to a silicate-bearing liquid together with other reduced volatile species (e.g., CH_4, NH_3, H_2S).

For example, Chachan and Stevenson (2018) provided a comprehensive analysis to estimate the relative distribution of H_2 in magma oceans and its retention in the atmosphere of rocky super Earths. These calculations were based on the planet's mass ($> 2\ M_\oplus$) and the thermal gradients established between the magma ocean and atmosphere. A crucial element of this approach involves employing H_2 solubility controls akin to noble gases, such as He, that anticipate a rise in solubility as temperature increases (Iacono-Marziano et al., 2010; Paonita, 2005). It is worth noting that the use of a noble gas-based approach to constrain H_2 solubility refers to anhydrous silicate melts. The results indicated a significant rise in the abundance of H_2 in the molten silicates compared to the overlying atmosphere, as the magma ocean's surface temperature (T_{sur}) and planetary mass (M_p) increased (Fig. 5a). Adopting our experimental data in these models, however, indicate the opposite.

To illustrate this, the fraction of H_2 dissolved in molten silicates relative to the atmosphere (M_{diss}/M_{atm}) is described as follows (Chachan and Stevenson, 2018):

$$M_{diss}/M_{atm} = (X_{H2}^{int} * M_p)/(f_{H2} * P_{sur} * (\frac{4\pi R_P^4}{G * M_p}) \tag{9}$$

where $X_{H_2}^{int}$ is the mole fraction of H_2 dissolved in the planet's interior, G is the gravitational constant, P_{sur} and R_p are the planet's atmospheric pressure at the surface of the magma ocean and radii, respectively. For the direct application of our experimentally derived empirical

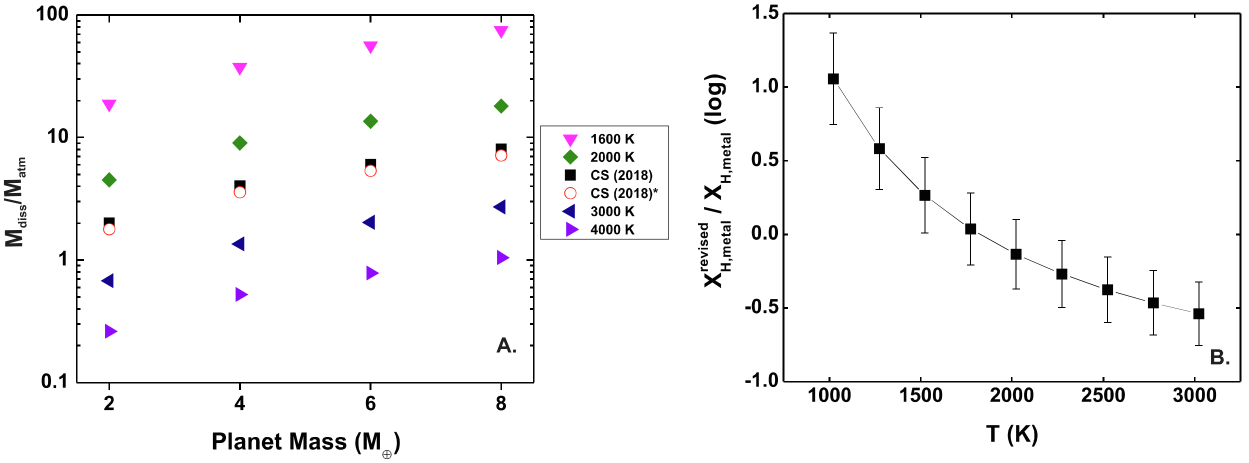

Fig. 5. Theoretical models involving the interaction of an H_2-bearing atmosphere with the surface of a magma ocean in a rocky planetary body. A) The fraction of H_2 dissolved in molten silicates relative to the atmosphere (M_{diss}/M_{atm}) is estimated as a function of magma ocean's surface temperature and planet's mass. The data shown for CS2018* correspond to the application of a P_{sur}-M_p relationship from Misener and Schlichting (2021) on the model of Chachan and Stevenson (2018) and for T_{sur} of 2000 K. Analysis suggests that the decrease in the solubility of H_2 in silicate liquid with temperature inferred from this experimental study could hinder the extent of H_2 fractionation between atmospheric envelopes and underlying magma oceans. At $T_{sur} > 3000$ K, the model suggests limited H transfer into planetary interior. B) The logarithmic ratio of $X_{H,metal}$ (revised) after considering the solubility of H_2 in silicate melt determined here (eq. 8) with the $X_{H,metal}$ estimations by Young et al. (2023) as a function of T_{sur}. Experimental data imply that for $X_{H,metal}$ comparable to those estimated for planetary embryos resembling early Earth, the H_2 in the atmospheric envelope must be increased tenfold in contrast to previous models (Young et al., 2023).

description of H_2 solubility in silicate melts (Eqn 8), we constrained the P_{sur} as a function of M_p by employing the relationships described in Misener and Schlichting (2021; eq. 29) and Young et al. (2023; eq. 26). Both methodologies produce comparable outcomes. Nevertheless, the formulation proposed by Misener and Schlichting (2021) aligns more closely with the model presented by Chachan and Stevenson (2018) (Fig. 5a). Here, the parameter T_o that defines the intermolecular interactions between H_2 and magma was set to 3000 K, as it appears to have a negligible difference compared to the value of 5000 K for $T_{sur} <$ 2500 K (Chachan and Stevenson, 2018).

For volatile solubility constrained by the temperature dependence defined by our experimental data, results indicate that the H_2 dissolved in a magma ocean with $T_{sur} = 2000$ K could be nearly 60 % higher than that predicted earlier (Chachan and Stevenson, 2018) (Fig. 5a). Moreover, as the T_{sur} increases, there is a noticeable decrease in H_2 melt concentrations. As such, if the surface conditions of the magma ocean surpass 4000 K (Bajgain et al., 2022), it could result in the magma ocean being undersaturated in H_2 compared to the atmosphere above (Fig. 5a), and thus, limiting the extent of H transfer in the planetary interior. It should be pointed out that these calculations, which do not require the implementation of the T_o parameter, were performed under temperature conditions that fall outside the range of applicability for the empirical equation that describes the solubility of H_2 in silicate melts (873–1723 K, Eqn 8), while assuming H_2 dissolution mechanisms similar to those discussed for H_2O-bearing silicate liquids.

One of the most recent evolution models for Earth-like planets has also utilized the same concept of atmospheric H_2 dissolution into early magma oceans to constrain mantle redox conditions and the relative abundance of H in metal cores (Young et al., 2023). The model argues that an atmospheric abundance of H_2 as low as 0.2 % mass fraction in a planetary embryo (0.5 $M_{\oplus}$)(Ginzburg et al., 2016) may be adequate to form a metal core with density that is similar to Earth's (Birch, 1964). Here, the reduced equation that links the partial pressure of atmospheric H_2 (f_{H_2}) at the interface with the magma ocean to the activity of H in the Fe metal (α_H) is as follows (Clesi et al., 2018; Young et al., 2023):

$$\alpha_H = \sqrt{K_H K^{m/f} f_{H2}} \quad (10)$$

where K_H is the equilibrium constant for H solubility between silicate liquid and Fe metal. This approach assumes that H mixes ideally with Fe liquid and exhibits a moderate siderophile behavior (Okuchi, 1997). It is worth noting, however, that recent experimental and theoretical studies have argued that H attains increased siderophile behavior under high pressures of metal-melt equilibration (Clesi et al., 2018; Li et al., 2020; Malavergne et al., 2019; Tagawa et al., 2021; Yuan and Steinle-Neumann, 2020), which could also be influenced by the degree of C saturation in the melt-metal system (see detailed discussion in Gaillard et al., 2022).

By acknowledging the uncertainty regarding the impact of pressure on H dissolution in liquid metal, incorporating our empirically derived $K^{m/f}$ (Eqn 8) in Eqn 10 results in a projected mole fraction of H in Fe metal ($X_{H,metal}$) that is more than 60 % lower than previous estimates for comparable f_{H_2} atmospheric conditions (Young et al., 2023). To this end, our experimental data imply that to achieve H mole fractions in planetary cores comparable to those proposed for Earth (0.5–0.8 wt%) and for a core-mantle boundary of planetary embryos at 3000 K, by following the evolution model of Young et al. (2023), f_{H_2} must be increased tenfold relative to what has been proposed (Fig. 5b). This corresponds to planetary embryos featuring primary atmospheres that are enriched with an approximate H_2 mass fraction of 2 %. If this hypothesis stands, then models regarding volatile retention in rocky exoplanets would need to be adjusted to accommodate greater degrees of H-bearing volatile depletion in the primordial atmospheric envelopes (Chachan and Stevenson, 2018; Kite and Schaefer, 2021; Misener and Schlichting, 2021).

When considering smaller objects like planetesimals, it is possible to formulate additional hypotheses regarding the redox conditions established in the early stages of solar system evolution. Several studies have modeled the redox conditions linked to primitive objects such as enstatite and CR chondrite chondrules (e.g., Grossman et al., 2008; Righter et al., 2016; Tenner et al., 2015) with estimated oxygen fugacity (f_{O_2}) values that were between 2 and 6 log units lower than the iron-wustite (IW) redox buffer. Here, an estimate is made of the degree of H_2 solubility in a chondrule melt when in equilibrium with the surrounding solar nebula. In this model, the partial pressure of H_2O (P_{H_2O}) and H_2 ($P_{H_2} = f_{H_2}$) are calculated by adopting the formulations outlined in Grossman et al. (2008). An important component in these models is the relative activity of $H_2O_{(g)}$ and $H_{2(g)}$ as described in equilibrium with $O_{2(g)}$:

$$H_2O_{(g)} = 1/2O_{2(g)} + H_{2(g)} \quad (11)$$

expressed with an equilibrium constant (K_w) defined as:

$$K_w = \left(P_{H_2O}/P_{H2}\right)\Big/ f_{O_2}^{0.5} \quad (12)$$

The P_{H_2O}/P_{H_2} ratios can be estimated by adopting various f_{O_2} conditions approximated for the solar nebula, Si/FeSi, and IW redox buffers (see Fig. 6a). The SiO_2/FeSi buffer is utilized as a model to represent suitable redox conditions for the Si content of metal grains in enstatite chondrites (Grossman et al., 2008; Lehner et al., 2013). Clearly, oxidizing conditions favor H_2O relative to H_2, with P_{H_2O} approaching P_{H_2} when the f_{O_2} approaches IW redox conditions. Under the extremely reducing conditions of a SiO_2/FeSi system, the P_{H_2O}/P_{H_2} ratio approximates those of a solar nebula at temperatures higher than 1600 K. Despite the wide range of redox and P_{H_2O}/P_{H_2} considered, this theoretical approach suggests that negligible amounts of solar nebula H_2 would have been dissolved in molten objects formed within the protoplanetary disk (Fig. 6b). Most importantly, the extent of H_2 incorporation depends proportionally on the P_{total} of the system, and thus it would be an order of magnitude lower for canonical solar nebula ($P_{total} = 10^{-4}$ atm). Thus, the pressure conditions within the protoplanetary disk should be more crucial for transferring nebular H_2 into silicate melts than the redox and P_{H_2O}/P_{H_2} conditions. Therefore, further analysis needs to be conducted alongside established sulfur fugacity conditions to elucidate the existence of highly reduced mineral phases in chondrules and enstatite chondrites (e.g., El Goresy et al., 2017; Grossman et al., 1985).

5. Conclusions

This study describes the equilibrium partitioning of molecular H_2 between H_2O-bearing aluminosilicate melts and aqueous solutions by employing in situ observations in a series of hydrothermal diamond anvil cell experiments. The equilibrium relationship between $H_{2(g)}$ and $H_{2(melt)}$ in the coexisting phases is described by an empirical approach that extends to 600–1450 °C; 0.3–3 GPa by incorporating data from previous experimental studies (Bezmen et al., 2011; Bezmen et al., 1991; Hirschmann et al., 2012; Mysen, 2018; Persikov et al., 1990). Results indicate that with H_2O-saturated melts, the behavior of H_2 follows Henrian behavior, similar to what is expected of inert, neutral non-polar species. To this end, the solubility of H_2 in the melt appears to be controlled by the mole fraction of H_2O while being hindered with the temperature increase. These results will enhance our understanding of H

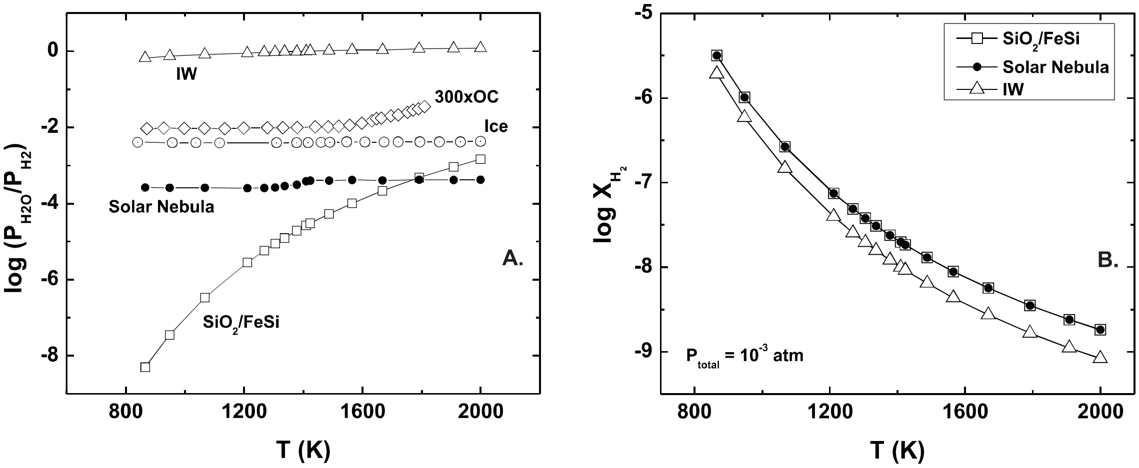

Fig. 6. A) The logarithmic ratio of partial pressures of H_2O and H_2 in a protoplanetary disk if buffered by SiO_2/FeSi and IW f_{O_2} conditions, compared to the ratios proposed for the solar nebula (Grossman et al., 2008). The estimated P_{H_2O}/P_{H_2} shown for disk enriched in water ice and dust of ordinary chondrite (OC) composition (300 times of solar composition) are nearly identical to those calculated by Grossman et al. (2008). Overall, redox conditions range from solar nebula conditions with pure gas composition to ones with significant dust enrichment (Ebel and Grossman, 2000; Tenner et al., 2015). B) Models that describe the mole fraction of H_2 in silicate melts (X_{H_2}) as a function of temperature by adopting the experimental data on H_2 melt solubility (eq. 8), propose a minimal dissolution of nebular H_2 in the molten surface of primitive chondritic parent bodies even under the extremely reducing conditions of a SiO_2/FeSi redox buffer. The model considers only H_2, H_2O and He (~0.2 P_{total}) for volatile components. Calculations consider the highest pressure for solar nebula envisioned (10^{-3} to 10^{-5} atm) to be consistent with the range of P_{H_2O}/P_{H_2} ratios discussed by Grossman et al. (2008). The SiO_2/FeSi redox conditions are estimated after Lehner et al. (2013), with $\log f_{O_2} = 8.59–42712/T$ for the temperature range of 1000–1850 K. The f_{O_2} for IW is from Myers and Eugster (1983). The equilibrium constant for H_2O dissociation is from Holland and Powell (1998).

evolution in the interior of Earth and potentially of rocky exoplanets through models that investigate the cycling of H between magma oceans and their surrounding atmospheres.

CRediT authorship contribution statement

Dionysis I. Foustoukos: Writing – review & editing, Writing – original draft, Visualization, Validation, Supervision, Software, Resources, Project administration, Methodology, Investigation, Funding acquisition, Formal analysis, Data curation, Conceptualization.

Data availability

The raw Raman vibrational spectra collected are available through Zenodo at https://doi.org/10.5281/zenodo.11527174.

Declaration of competing interest

The authors declare that they have no known competing financial interests or personal relationships that could have appeared to influence the work reported in this paper.

Acknowledgments

This research was conducted with support from the NSF-EAR-1761388 and the NSF-OCE-2308386. I am thankful to Yufei Meng and Joseph Lai for providing ultrapure CVD diamonds; and to Bjorn Mysen, George Cody and Conel Alexander for providing thoughtful and intellectually stimulating discussions. Constructive reviews were provided by Celia Dalou, Fabrice Gaillard, Mathieu Roskosz, and an anonymous reviewer. This study pays tribute to the memory of Ioannis Chrysostomos Foustoukos (1947-2024), my beloved father.

Appendix A. Supplementary material

This file contains: data from models regarding the properties of sodium aluminosilicate melts associated with the effects of H_2O dissolution in melt structure (Table S1-S4, Figure S1); the Q^n speciation and NBO/T of the NA10 melts in Exp#3 (Tabel S5); thermodynamic properties for the $H_{2(g)} = H_{2(melt)}$ equilibrium (Table S6); the relationships between the mole fraction of H_2O in melts and the NBO/T (Figure S2) and the Henry's law constant of H_2 solubility in the silicate melts (Figure S3); and an example of the curve-fitting approach employed on Raman spectra collected. Supplementary material to this article can be found online at https://doi.org/10.1016/j.gca.2024.10.020.

References

Anderson, G.M., Crerar, D., 1993. Thermodynamics in Geochemistry - The Equilibrium Model. Oxford University Press, New York Oxford.

Aranovich, L.Y., Newton, R.C., 1996. H_2O activity in concentrated NaCl solutions at high pressures and temperatures measured by the brucite-periclase equilibrium. Contrib. Miner. Petrol. 125, 200–212.

Bajgain, S.K., Ashley, A.W., Mookherjee, M., Ghosh, D.B., Karki, B.B., 2022. Insights into magma ocean dynamics from the transport properties of basaltic melt. Nat Commun 13. Artn 7590.

Bassett, W.A., Wu, T.C., Chou, I.M., Haselton, H.T., Jr., Frantz, J., Mysen, B.O., Huang, W.L., Sharma, K. and Schiferl, D., 1996. The hydrothermal diamond anvil cell (HDAC) and its applications. In: Dyar, M.D., McCammon C., Schaefe, W.M. (Eds.), Mineral Spectroscopy: A Tribute to Roger G. Burns. The Geochemical Society Special Publication, No. 5, pp. 261–272.

Bezmen, N.I., Zharikov, V.A., Epelbaum, M.B., Zavelsky, V.O., Dikov, Y.P., Suk, N.I., Koshemchuk, S.K., 1991. The system $NaAlSi_3O_8$ - H_2O–H_2 (1200 °C, 2 kbar) - the solubility and interaction mechanism of fluid species with melt. Contrib. Miner. Petrol. 109, 89–97.

Bezmen, N.I., Zavel'sky, V.O., Salova, T.P., 2011. Solubility of water-hydrogen fluid in haplogranite, albite, and sodium disilicate melts. Petrology 19, 183–197.

Birch, F., 1964. Density and composition of mantle and core. J. Geophys. Res. 69, 4377–4388.

Burnham, C.W., Davis, N.F., 1974. Role of H_2O in silicate melts.2. Thermodynamic and phase relations in system $NaAlSi_3O_8$-H_2O to 10 kilobars, 700 °C to 1100 °C. Am. J. Sci. 274, 902–940.

Canup, R.M., 2012. Forming a moon with an Earth-like composition via a giant impact. Science 338, 1052–1055.

Carroll, M.R., Stolper, E.M., 1993. Noble-gas solubilities in silicate melts and glasses - New experimental results for argon and the relationship between solubility and ionic porosity. Geochim. Cosmochim. Acta 57, 5039–5051.

Chachan, Y., Stevenson, D.J., 2018. On the role of dissolved gases in the atmosphere retention of low-mass low-density planets. Astrophys J 854. Artn 21.

Cheng, N., Chou, I.M., Wan, Y., Wang, R., Zhang, H., Chen, Y., 2023. The intrinsic effects of using rhenium gaskets in hydrothermal diamond anvil cell experiments on background fluorescence, contamination, and redox control. Chem. Geol. 632, 121535.

Clesi, V., Bouhifd, M.A., Bolfan-Casanova, N., Manthilake, G., Schiavi, F., Raepsaet, C., Bureau, H., Khodja, H., Andrault, D., 2018. Low hydrogen contents in the cores of terrestrial planets. Sci Adv 4. Artn e1701876.

Cody, G.D., Mysen, B.O., Lee, S.K., 2005. Structure vs. composition: A solid-state ^{1}H and ^{29}Si NMR study of quenched glasses along the Na_2O-SiO_2-H_2O join. Geochim. Cosmochim. Acta 69, 2373–2384.

Cook, D.R., Weisberg, S., 1999. Applied regression including computing and graphics. Wiley-Interscience.

Dalou, C., Le Losq, C., Furi, E., Caumon, M.C., 2022. Redox controls on H and N speciation and intermolecular isotopic fractionations in aqueous fluids at high pressure and high temperature: Insights from in situ experiments. Front Earth Sc-Switz 10. Artn 973802.

Devore, J.L., 1995. Probability and statistics for engineering and the sciences. Duxbury Press.

Doremus, R.H., 1966. Physical solubility of gases in fused silica. J. Am. Ceram. Soc. 49, 461–462.

Ebel, D.S., Grossman, L., 2000. Condensation in dust-enriched systems. Geochim. Cosmochim. Acta 64, 339–366.

El Goresy, A., Lin, Y., Miyahara, M., Gannoun, A., Boyet, M., Ohtani, E., Gillet, P., Trieloff, M., Simionovici, A., Feng, L., Lemelle, L., 2017. Origin of EL3 chondrites: Evidence for variable C/O ratios during their course of formation: A state of the art scrutiny. Meteorit. Planet. Sci. 52, 781–806.

Fine, G., Stolper, E., 1986. Dissolved carbon dioxide in basaltic glasses: concentrations and speciation. Earth Planet. Sci. Lett. 76, 263–278.

Foustoukos, D.I., 2016a. On the ionic strength and electrial conductivity of crustal brines. Chem. Geol. 447, 183–190.

Foustoukos, D.I., 2016b. On the solvation properties of supercritical electrolyte solutions. Chem. Geol. 447, 191–198.

Foustoukos, D.I., 2019. Hydrothermal oxidation of Os. Geochim. Cosmochim. Acta 255, 237–246.

Foustoukos, D.I., Mysen, B.O., 2012. D/H fractionation in the H_2–H_2O system at supercritical water conditions: Compositional and hydrogen bonding effects. Geochim. Cosmochim. Acta 86, 88–102.

Foustoukos, D.I., Mysen, B.O., 2013. H/D methane isotopologues dissolved in magmatic fluids: Stable hydrogen isotope fractionations in the Earth's interior. Am. Mineral. 98, 946–954.

Foustoukos, D.I., Mysen, B.O., 2015. The structure of water-saturated carbonate melts. Am. Mineral. 100, 35–46.

Gaillard, F., Schmidt, B., Mackwell, S., McCammon, C., 2003. Rate of hydrogen-iron redox exchange in silicate melts and glasses. Geochim. Cosmochim. Acta 67, 2427–2441.

Gaillard, F., Malavergne, V., Bouhifd, M.A., Rogerie, G., 2022. A speciation model linking the fate of carbon and hydrogen during core - magma ocean equilibration. Earth Planet. Sci. Lett. 577. Artn 117266.

Ginzburg, S., Schlichting, H.E., Sari, R., 2016. Super-Earth atmospheres: Self-consistent gas accretion and retention. Astrophys J 825. Artn 29.

Grossman, L., Beckett, J.R., Fedkin, A.V., Simon, S.B., Ciesla, F.J., 2008. Redox conditions in the solar nebula: Observational, experimental, and theoretical constraints. Oxygen Solar Syst. 68, 93–140.

Grossman, J.N., Rubin, A.E., Rambaldi, E.R., Rajan, R.S., Wasson, J.T., 1985. Chondrules in the Qingzhen type-3 enstatite chondrite - Possible precursor components and comparison to ordinary chondrite chondrules. Geochim. Cosmochim. Acta 49, 1781–1795.

Guice, G.L., Ackerson, M.R., Holder, R.M., George, F.R., Browning-Hanson, J.F., Burgess, J.L., Foustoukos, D.I., Becker, N.A., Nelson, W.R., Viete, D.R., 2021. Suprasubduction zone ophiolite fragments in the central Appalachian orogen: Evidence for mantle and Moho in the Baltimore Mafic Complex (Maryland, USA). Geosphere 17. https://doi.org/10.1130/GES02289.1.

Hayatsu, A., Waboso, C.E., 1985. The solubility of rare gases in silicate melts and implications for K-Ar dating. Chem. Geol. 52, 97–102.

Hirschmann, M.M., Withers, A.C., Ardia, P., Foley, N.T., 2012. Solubility of molecular hydrogen in silicate melts and consequences for volatile evolution of terrestrial planets. Earth Planet. Sci. Lett. 345, 38–48.

Holland, T.J.B., Powell, R., 1998. An internally consistent thermodynamic data set for phases of petrological interest. J. Metam. Geol. 16, 309–343.

Holloway, J.R., Blank, J.G., 1994. Application of experimental results to C-O-H species in natural melts. Rev Mineral 30, 187–230.

Iacono-Marziano, G., Paonita, A., Rizzo, A., Scaillet, B., Gaillard, F., 2010. Noble gas solubilities in silicate melts: New experimental results and a comprehensive model of the effects of liquid composition, temperature and pressure. Chem. Geol. 279, 145–157.

Kennedy, G.C., Heard, H.C., Wasserburg, G.J., Newton, R.C., 1962. Upper 3-phase region in system SiO_2-H_2O. Am. J. Sci. 260, 501–521.

Kite, E.S., Schaefer, L., 2021. Water on hot rocky exoplanets. Astrophys J Lett 909. Artn L22.

Le Losq, C., Cody, G.D., Mysen, B.O., 2015. Alkali influence on the water speciation and the environment of protons in silicate glasses revealed by H-1 MAS NMR spectroscopy. Am. Mineral. 100, 466–473.

Le Losq, C., Dalou, C., Mysen, B.O., 2017. In situ study at high pressure and temperature of the environment of water in hydrous Na and Ca aluminosilicate melts and coexisting aqueous fluids. J. Geophys. Res. Solid Earth 122, 4888–4899.

Lee, R.W., 1963. Diffusion of hydrogen in natural and synthetic fused quartz. J. Chem. Phys. 38, 448–455.

Lehner, S.W., Petaev, M.I., Zolotov, M.Y., Buseck, P.R., 2013. Formation of niningerite by silicate sulfidation in EH3 enstatite chondrites. Geochim. Cosmochim. Acta 101, 34–56.

Li, Y.G., Vocadlo, L., Sun, T., Brodholt, J.P., 2020. The Earth's core as a reservoir of water. Nat Geosci 13, 453–458.

Lissauer, J.J., Batalha, N.M., Borucki, W.J., 2023. Exoplanet Science from Kepler. In: Inutsuka, S., Aikawa, Y., Muto, T., Tomida, K., Tamura, M. (Eds.), Protostars and Planets VII. Kyoto, Japan, p. 839.

Long, D.A., 1977. Raman spectroscopy. MgGraw-Hill, New York.

Luth, R.W., Boettcher, A.L., 1986. Hydrogen and the melting of silicates. Am. Mineral. 71, 264–276.

Luth, R.W., Mysen, B.O., Virgo, D., 1987. Raman spectroscopic study of the solubility behavior of H_2 in the system Na_2O-Al_2O_3-SiO_2-H_2. Am. Mineral. 72, 481–486.

Lux, G., 1987. The behavior of noble gases in silicate liquids - solution, diffusion, bubbles and surface effects, with applications to natural samples. Geochim. Cosmochim. Acta 51, 1549–1560.

Malavergne, V., Bureau, H., Raepsaet, C., Gaillard, F., Poncet, M., Surblé, S., Sifré, D., Shcheka, S., Fourdrin, C., Deldicque, D., Khodja, H., 2019. Experimental constraints on the fate of H and C during planetary core-mantle differentiation. Implications for the Earth. Icarus 321, 473–485.

Meng, Y.F., Yan, C.S., Krasnicki, S., Liang, Q., Lai, J., Shu, H.Y., Yu, T., Steele, A., Mao, H. K., Hemley, R.J., 2012. High optical quality multicarat single crystal diamond produced by chemical vapor deposition. Phys. Status Solidi A-Appl. Mater. Scie. 209, 101–104.

Misener, W., Schlichting, H.E., 2021. To cool is to keep: residual H/He atmospheres of super-Earths and sub-Neptunes. Mon. Not. R Astron. Soc. 503, 5658–5674.

Montana, A., Guo, Q.T., Boettcher, S., White, B.S., Brearley, M., 1993. Xe and Ar in high-pressure silicate liquids. Am. Mineral. 78, 1135–1142.

Moore, G., Vennemann, T., Carmichael, I.S.E., 1995. Solubility of water in magmas to 2 kbar. Geology 23, 1099–1102.

Moore, G., Vennemann, T., Carmichael, I.S.E., 1998. An empirical model for the solubility of H_2O in magmas to 3 kilobars. Am. Mineral. 83, 36–42.

Mordasini, C., Burn, R., 2024. Planet formation – observational constraints, physical processes, and compositional patterns, p. arXiv:2404.15555, https://doi.org/10.48550/arXiv.2404.15555.

Myers, J., Eugster, H.P., 1983. The system Fe-Si-O - oxygen buffer calibrations to 1,500 K. Contrib. Miner. Petrol. 82, 75–90.

Mysen, B.O., 2009. Solution mechanisms of silicate in aqueous fluid and H_2O in coexisting silicate melts determined in situ at high pressure and high temperature. Geochim. Cosmochim. Acta 73, 5748–5763.

Mysen, B.O., 2010. Structure of H_2O-saturated peralkaline aluminosilicate melt and coexisting aluminosilicate-saturated aqueous fluid determined in situ to 800 ^{o}C and 800 MPa. Geochim. Cosmochim. Acta 74, 4123–4139.

Mysen, B.O., 2012. High-pressure and high-temperature titanium solution mechanisms in silicate-saturated aqueous fluids and hydrous silicate melts. Am. Mineral. 97, 1241–1251.

Mysen, B.O., 2013a. Effects of fluid and melt density and structure on high pressure and temperature experimental studies of hydrogen isotope partitioning between coexisting melt and aqueous fluid. Am. Mineral. 98, 1754–1764.

Mysen, B.O., 2013b. Hydrogen isotope fractionation between coexisting hydrous melt and silicate-saturated aqueous fluid: An experimental study in situ at high pressure and temperature. Am. Mineral. 98, 376–386.

Mysen, B.O., 2018. Solution mechanisms of COHN fluids in melts to upper mantle temperature, pressure, and redox conditions. Am. Mineral. 103, 1780–1788.

Mysen, B.O., Acton, M., 1999. Water in H_2O-saturated magma-fluid systems: Solubility behavior in K_2O-Al_2O_3-SiO_2-H_2O to 2.0 GPa and 1300 ^{o}C. Geochim. Cosmochim. Acta 63, 3799–3815.

Mysen, B.O., Richet, P., 2005. Silicate Glasses and Melts - Properties and Structure. Elsevier, New York.

Mysen, B.O., Virgo, D., 1986. Volatiles in silicate melts at high pressure and temperature: 1. Interaction between OH groups and Si^{4+}, Al^{3+}, Ca^{2+}, Na^+ and H^+. Chem. Geol. 57, 303–331.

Mysen, B.O., Yamashita, S., 2010. Speciation and solubility of reduced C-O-H fluids in coexisting fluids and silicate melts determined in situ to 1.45 GPa and 800°C. Geochim. Cosmochim. Acta 74, 4577–4588.

Nakamura, Y., 1974 The system SiO_2-H_2O-H_2 at 15 kbar. Carnegie Institution of Washington Year Book 73, 259-263.

Nuccio, P.M., Paonita, A., 2000. Investigation of the noble gas solubility in H_2O-CO_2 bearing silicate liquids at moderate pressure II: the extended ionic porosity (EIP) model. Earth Planet. Sci. Lett. 183, 499–512.

Okuchi, T., 1997. Hydrogen partitioning into molten iron at high pressure: Implications for Earth's core. Science 278, 1781–1784.

Paonita, A., 2005. Noble gas solubility in silicate melts: a review of experimentation and theory, and implications regarding magma degassing processes. Ann. Geophys.-Italy 48, 647–669.

Paonita, A., Gigli, G., Gozzi, D., Nuccio, P.M., Trigila, R., 2000. Investigation of the He solubility in H_2O-CO_2 bearing silicate liquids at moderate pressure: a new experimental method. Earth Planet. Sci. Lett. 181, 595–604.

Persikov, E.S., Zharikov, V.A., Bukhtiyarov, P.G., Polskoy, S.F., 1990. The effect of volatiles on the properties of magmatic melts. Eur. J. Mineral. 2, 621–642.

Press, W.H., Teukolsky, S.A., Vetterling, W.T. and Flannery, B.P. (2007) Numerical recipes in C: The art of scientific computing, Third ed. Cambridge University Press, p. 661-666.

Press, C.R.C. (2016) CRC handbook of chemistry and physics online, Handbook of chemistry and physics. CRC Press, Boca Raton, FL.

Righter, K., Sutton, S.R., Danielson, L., Pando, K., Newville, M., 2016. Redox variations in the inner solar system with new constraints from vanadium XANES in spinels. Am. Mineral. 101, 1928–1942.

Schiferl, D., Nicol, M., Zaug, J.M., Sharma, S.K., Cooney, T.F., Wang, S.-Y., Anthony, T. R., Fleischer, J.F., 1997. The diamond $^{13}C/^{12}C$ isotope Raman pressure sensor system for high temperature/pressure diamond-anvil cells with reactive samples. J. Appl. Phys. 82, 3256–3265.

Schmidt, B.C., Holtz, F., Scaillet, B., Pichavant, M., 1997. The influence of H_2O–H_2 fluids and redox conditions on melting temperatures in the haplogranite system. Contrib. Miner. Petrol. 126, 386–400.

Schmidt, B.C., Holtz, F.M., Beny, J.M., 1998. Incorporation of H_2 in vitreous silica, qualitative and quantitative determination from Raman and infrared spectroscopy. J Non-Cryst Solids 240, 91–103.

Schmidt, B.C., Holtz, F., Pichavant, M., 1999. Water solubility in haplogranitic melts coexisting with H_2O–H_2 fluids. Contrib. Miner. Petrol. 136, 213–224.

Shackelford, J.F., Studt, P.L., Fulrath, R.M., 1972. Solubility of gases in glass II. He, Ne, and H_2 in fused silica. J. Appl. Phys. 43, 1619–1626.

Shang, L.B., Chou, I.M., Lu, W.J., Burruss, R.C., Zhang, Y.X., 2009. Determination of diffusion coefficients of hydrogen in fused silica between 296 and 523 K by Raman spectroscopy and application of fused silica capillaries in studying redox reactions. Geochim. Cosmochim. Acta 73, 5435–5443.

Shibata, T., Takahashi, E., Matsuda, J., 1998. Solubility of neon, argon, krypton, and xenon in binary and ternary silicate systems: A new view on noble gas solubility. Geochim. Cosmochim. Acta 62, 1241–1253.

Shinozaki, A., Kagi, H., Noguchi, N., Hirai, H., Ohfuji, H., Okada, T., Nakano, S., Yagi, T., 2014. Formation of SiH_4 and H_2O by the dissolution of quartz in H_2 fluid under high pressure and temperature. Am. Mineral. 99, 1265–1269.

Sverjensky, D.A., Harrison, B., Azzolini, D., 2014. Water in the deep Earth: The dielectric constant and the solubilities of quartz and corundum to 60 kb and 1200 ^{o}C. Geochim. Cosmochim. Acta 129, 125–145.

Tagawa, S., Sakamoto, N., Hirose, K., Yokoo, S., Hernlund, J., Ohishi, Y., Yurimoto, H., 2021. Experimental evidence for hydrogen incorporation into Earth's core. Nat Commun 12. Artn 2588.

Teal, G.K., MacWood, G.E., 1935. The Raman spectra of the isotopic molecules H_2, HD, and D_2. J. Chem. Phys. 3, 760–764.

Tenner, T.J., Nakashima, D., Ushikubo, T., Kita, N.T., Weisberg, M.K., 2015. Oxygen isotope ratios of FeO-poor chondrules in CR3 chondrites: Influence of dust enrichment and H_2O during chondrule formation. Geochim. Cosmochim. Acta 148, 228–250.

Veirs, D.K., Rosenblatt, G.M., 1987. Raman line positions in molecular hydrogen - H_2, HD, HT, D_2, DT, and T_2. J Mol Spectrosc 121, 401–419.

Vlasov, K., Audetat, A., Keppler, H., 2023. H_2–H_2O immiscibility in Earth's upper mantle. Contrib. Miner. Petrol. 178. Artn 36.

Weiss, L.M., Millholland, S.C., Petigura, E.A., Adams, F.C., Batygin, K., Block, A.M., Mordasini, C., 2023. Architectures of compact multi-planet systems: Diversity and uniformity. In: Inutsuka, S., Aikawa, Y., Muto, T., Tomida, K., Tamura, M. (Eds.), Protostars and Planets VII. Kyoto, Japan, p. 863.

White, B.S., Brearley, M., Montana, A., 1989. Solubility of argon in silicate liquids at high-pressures. Am. Mineral. 74, 513–529.

Williams, K.A., Pradhan, B.K., Eklund, P.C., Kostov, M.K., Cole, M.W., 2002. Raman spectroscopic investigation of H_2, HD, and D_2 physisorption on ropes of single-walled, carbon nanotubes. Phys Rev Lett 88. Artn 165502.

York, D., 1969. Least squares fitting of a straight line with correlated errors. Earth Planet. Sci. Lett. 5, 320–324.

Young, E.D., Shahar, A., Schlichting, H.E., 2023. Earth shaped by primordial H atmospheres. Nature 616, 306–311.

Yuan, L., Steinle-Neumann, G., 2020. Strong sequestration of hydrogen Into the Earth's core during planetary differentiation. Geophys. Res. Lett. 47. Artn e2020GL088303.

Zhang, Y.X., Ni, H.W., 2010. Diffusion of H, C, and O components in silicate melts. Diffusion Minerals Melts 72, 171–225.

Zotov, N., Keppler, H., 2002. Silica speciation in aqueous fluids at high pressures and high temperatures. Chem. Geol. 184, 71–82.